Laser thermoelastic generation in metals above the melt threshold

A. G. Every, Z. N. Utegulov, and I. A. Veres

Citation: Journal of Applied Physics **114**, 203508 (2013); doi: 10.1063/1.4832483
View online: https://doi.org/10.1063/1.4832483
View Table of Contents: http://aip.scitation.org/toc/jap/114/20
Published by the American Institute of Physics

Laser thermoelastic generation in metals above the melt threshold

A. G. Every,[1] Z. N. Utegulov,[2] and I. A. Veres[3]
[1]*School of Physics, University of the Witwatersrand, PO Wits 2050, South Africa*
[2]*Department of Physics, School of Science and Technology, Nazarbayev University, Astana 010000, Kazakhstan*
[3]*RECENDT Research Center for Non-Destructive Testing GmbH, A-4040 Linz, Austria*

(Received 16 August 2013; accepted 6 November 2013; published online 27 November 2013)

An approach is presented for calculating thermoelastic generation of ultrasound in a metal plate exposed to nanosecond pulsed laser heating, sufficient to cause melting but not ablation. Detailed consideration is given to the spatial and temporal profiles of the laser pulse, penetration of the laser beam into the sample, the appearance and subsequent growth and then contraction of the melt pool, and the time dependent thermal conduction in the melt and surrounding solid throughout. The excitation of the ultrasound takes place during and shortly after the laser pulse and occurs predominantly within the thermal diffusion length of a micron or so beneath the surface. It is shown how, because of this, the output of the thermal simulations can be expressed as axially symmetric transient radial and normal surface force distributions. The epicentral displacement response to these force distributions is obtained by two methods, the one based on the elastodynamic Green's functions for plate geometry determined by the Cagniard generalized ray method and the other using a finite element numerical method. The two approaches are in very close agreement. Numerical simulations are reported on the epicentral displacement response of a 3.12 mm thick tungsten plate irradiated with a 4 ns pulsed laser beam with Gaussian spatial profile, at intensities below and above the melt threshold. [http://dx.doi.org/10.1063/1.4832483]

I. INTRODUCTION

There is an extensive literature on pulsed laser generation of ultrasound in opaque solids that explores in depth the surface thermoelastic and ablative regimes, see, e.g., Refs. 1–9. In contrast, little has been reported on ultrasound generation in the intermediate regime where the laser pulse energy is sufficient to cause near-surface melting but is below the vaporization threshold. The few notable publications in this area are the study of melting on the excitation of surface acoustic wave pulses in silicon by Gusev *et al.*[10] and the investigations of Mesaros *et al.*[11] and Reese *et al.*[12] on laser ultrasound transmission through a plate in the melting regime. There is need for a better understanding of this intermediate regime, because laser ultrasound provides a non-contact approach for studying melting and re-solidification both on short time scales and in hostile environments.

This paper reports on numerical simulations conducted to determine the epicentral displacement response of a metal plate exposed to nanosecond pulsed laser heating of the surface near the melt threshold. Because of the availability of experimental data on tungsten to compare with,[12] the simulations are performed on that refractory metal. However, our approach is quite general and is applicable to a wide range of opaque materials subjected to nanosecond pulsed laser heating.

At the outset, the thermoelastic equations are uncoupled to permit the thermal transport and progress of melting to be calculated and the thermal stresses arising thereby determined. These stresses are then fed into elastodynamic calculations to obtain the epicentral displacement response. The reverse effect of the influence of the dynamic displacement field on the thermal processes is less pronounced and is not considered here. A challenging numerical problem is posed by the vastly different spatial scales of the thermal and elastodynamic fields. For comparison with available experimental data,[12] the simulations have been performed on a 3.12 mm thick tungsten specimen exposed to a nanosecond laser pulse with Gaussian spatial profile. It will be shown that the thermal diffusion length for this situation is on the order of a micron. To take account of the finite optical penetration of the laser radiation into the tungsten, the temporal profile of the laser pulse requires spatial discretization of the order of 1 nm. The dynamic displacement field on the other hand extends through the 3.12 mm thick specimen and displays spatial variation on this much larger scale. If a common spatial grid were to be adopted for both the thermal and the elastodynamic simulations, the computational cost in the two or three dimensional case would be exorbitant.

The main thrust of this paper is to show how the calculation of the thermal and elastodynamic fields can be separated. The thermal simulations are conducted on the required fine grid for a thin sub-surface layer, and the outcome expressed in the form of radially symmetric time-dependent distributions of surface forces parallel and normal to the illuminated surface. The epicentral displacement response to these force distributions is then calculated by two methods, the first on the basis of elastodynamic Green's functions evaluated using the Cagniard generalized ray method, and second using finite element (FEM) simulations. The two approaches are in very close agreement.

The thermal simulations establish the detailed thermal spatio-temporal evolution of the irradiated sample due to the incidence of a laser pulse, including the temperature rise of

the solid phase preceding the melting, and the appearance, subsequent growth, and then contraction and disappearance of the melt pool due to re-solidification. We identify three evolving stress regimes: (1) presence of lateral compressive stress in solid that has undergone heating but not melting, (2) absence of lateral stress in the molten metal, and (3) presence of lateral tensile stress in re-solidified and cooling solid. The gradient of the lateral stress, integrated over depth, represents the evolving radial force distribution, which can be regarded as acting at the surface. The epicentral displacement response at the opposite side of the plate to this force distribution has the well-known characteristic shape for a surface thermoelastic source, with rounded discontinuities at the longitudinal/primary (P) and shear/secondary (S) wave arrivals. We show how the normal force distribution arises from the rapid local expansion and contraction normal to the surface and can be expressed as an integral over depth of a function which depends on the evolving local temperature. The normal force distribution gives rise to the co-called precursor, a prominent narrow pulse at the P arrival, and a small displacement at the S arrival. The shape of the precursor is roughly bipolar, but when combined with the broad component of the epicentral displacement due to the radial force distribution, it appears more akin to a positive monopolar pulse combined with a rounded negative step.

II. THERMAL SIMULATIONS

The thermal simulations reported here are aimed at demonstrating how thermoelastic generation in the melt regime can be calculated. For illustrative proposes, they are based on experimental parameters of Reese *et al.*[12] and somewhat idealized assumptions regarding the thermophysical properties of tungsten. The simulations are performed on a tungsten plate of thickness $h = 3.12$ mm. The surface region exposed to the laser pulse is cylindrically symmetric, with the absorbed heat flux in W/m^2 being

$$I(r,t) = \left(J\chi/\pi d^2\right)\exp\left(-r^2/d^2\right)f(t), \tag{1}$$

where J is the incident pulse energy, which ranges between 4 mJ and 10 mJ, $\chi = 0.45$ is the assumed temperature independent optical absorptivity of tungsten, $d = 0.354$ mm is one of the beam radii employed in the experiments of Ref. 12, r is the radial distance from the beam axis, and $f(t)$ is the normalized temporal pulse shape for a Nd:YAG pulsed laser shown in Figure 1. The absorbed pulse energy is the heat flux integrated over time and area

$$J\chi = \int_0^\infty 2\pi r dr \int_0^\infty dt I(r,t). \tag{2}$$

The optical penetration depth of the 532 nm laser pulse in tungsten, using data from Larrabee,[13] is

$$\eta = \frac{\lambda}{2\pi}\sqrt{2/\kappa''} = \frac{532}{2\pi}\sqrt{2/30} = 22\,\text{nm}, \tag{3}$$

with the energy deposition rate per unit volume with depth z given by

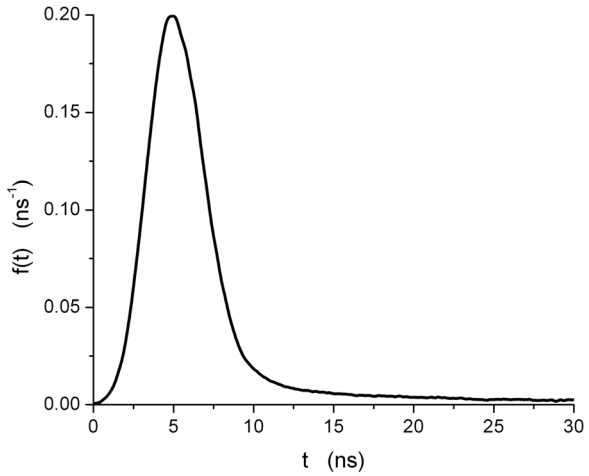

FIG. 1. Normalized typical temporal pulse shape $f(t)$ for a Nd:YAG pulsed laser used in these calculations. The pulse has full width at half maximum of about 4 ns and with maximum occurring at 5 ns after triggering, and there is a tail extending to about 30 ns.

$$P(r,z,t) = \frac{I(r,t)}{\eta}\exp(-z/\eta). \tag{4}$$

The density of tungsten is $\rho = 19\,300$ kg/m^3 at room temperature. There is a degree of variability of the other thermophysical properties depending on the particular tabulation consulted, temperature of measurement, and so on, see, e.g., Refs. 14–16, and so we have adopted reasonably typical values, taking the thermal conductivity to be $K = 173$ W/m °C, and well away from the melting point, the linear and volumetric thermal expansion coefficients to be $\alpha_0 = 4.3 \times 10^{-6}\,^\circ\text{C}^{-1}$ and $\beta_0 = 12.9 \times 10^{-6}\,^\circ\text{C}^{-1}$ respectively and the specific heat to be $c_0 = 131$ J/kg °C, all of these assumed to be the same in both the solid and liquid phases. The melting temperature of tungsten is nominally $T_m = 3410\,^\circ$C, but because of the inhomogeneity of the samples on a micro-scale and the rapidity of the heating and cooling in the laser experiments, with likely overheating and under-cooling,[17] the actual process of melting and solidification can reasonably be assumed to be spread over a finite temperature range. Accordingly, we take the latent heat of fusion, L_f and volume change on melting, V_{sl}, to be spread over a 200 °C temperature interval and combine these respectively with the specific heat and volumetric expansion coefficient, by treating the latter as the temperature-dependent quantities

$$c(T) = c_0 + L_f f(T), \tag{5}$$

where $c_0 = 131$ J/kg °C and $L_f = 184\,000$ J/kg and

$$\beta(T) = \beta_0 + V_{sl} f(T), \tag{6}$$

where $\beta_0 = 12.9 \times 10^{-6}\,^\circ\text{C}^{-1}$, and

$$f(T) = \begin{cases} \left\{1 + \cos\left(\pi(T - T_m)/100\right)\right\}/200, & |T - T_m| < 100\,^\circ\text{C} \\ 0, & |T - T_m| > 100\,^\circ\text{C} \end{cases} \tag{7}$$

is a smooth function peaking at T_m that integrates to unity. Reliable data on the value of V_{sl} for tungsten are not

available, so simulations have been done for V_{sl} ranging up to 0.04, i.e., a 4% change in volume on melting, which is a fairly typical value for many metals.[18]

The longitudinal wave speed is assumed to remain constant at the value $c_L = 5570$m/s, with the associated elastic modulus $C_{11} = \rho c_L^2 = 599$ GPa in both the solid and liquid phases. It is a common observation that the shear or transverse wave speed c_T and shear modulus $\mu = \rho c_T^2$ of the solid phase of a metal, on the other hand, softens on approach to the melting point and is then zero in the liquid phase. If μ were still to be finite in the temperature interval in which melting occurs and where β is very large, the lateral compressive stress generated would become un-physically large. It is reasonable therefore to assume that the shear wave speed starting at $c_T^0 = 3089$ m/s at room temperature, and shear modulus, vanish before melting actually starts, and so we take the temperature dependence of the shear modulus to fall smoothly to zero in the 200 °C interval preceding the start of melting by setting

$$\mu(T) = \mu_0 g(T), \tag{8}$$

where $\mu_0 = \rho(c_T^0)^2 = 193000 \times 3089^2 = 184.2$ GPa and

$$g(T) = \begin{cases} 1, & T < T_m - 300\,^\circ\text{C} \\ 0.5(1 - \sin(\pi(T - Tm + 200)/200), & T - 300\,^\circ\text{C} < T < T - 100\,^\circ\text{C} \\ 0, & T > T_m - 100\,^\circ\text{C}. \end{cases} \tag{9}$$

Away from the melting point, where the thermal diffusivity for tungsten is $\kappa = K/\rho c = 68.4 \times 10^{-6}$ m^2/s, the thermal diffusion length for a $\tau = 4$ ns heat pulse is

$$\ell = \sqrt{4\kappa\tau} = \sqrt{4 \times 68.4 \times 10^{-6}\text{m}^2/\text{s} \times 4 \times 10^{-9}\text{s}} = 1046\,\text{nm} = 1.046\,\mu\text{m}.$$

Since the optical penetration depth and thermal diffusion length are very much smaller than the beam radius, d, there is little lateral heat conduction, and for each value of r, the heat transport *can be treated as a 1D problem of heat flow normal to the sample surface*, depending on the time dependent laser intensity at the value of r. This is solved by discretizing the heat conduction equation, taking into account the melting that occurs when the local temperature reaches the melting point. The inherent nonlinearity of the problem due to the temperature dependence of the thermophysical properties is overcome by taking sufficiently small time steps.

Considering thermal conduction normal to the surface, the energy deposition rate from the penetrating laser beam $P(r, z, t)$ for given laser pulse energy and position r on the surface, and the temperature-dependent thermophysical properties of the medium, the spatio-temporal variation of the temperature $T(r, z, t)$ is governed by the 1D partial differential equation[6,19]

$$\frac{\partial T}{\partial t} = \kappa \frac{\partial^2 T}{\partial z^2} + \frac{P(r, z, t)}{\rho c} \tag{10}$$

and subject to Neumann boundary condition expressing absence of heat conduction across free surfaces, $\frac{\partial T}{\partial z}|_{z=0} = 0$. Discretizing the heat flow equation for a given $J\chi$ and r is implemented as follows:

$$z \to n\delta z,\ t \to i\delta t,\ n, i = 0, 1, 2, 3..., \tag{11}$$

$$T(z, t) \to T(n, i), \tag{12}$$

$$P(z, t) \to \frac{I(i)}{\eta}\exp(-n\delta z/\eta), \quad \kappa \to \kappa(T(n, i)), \quad c \to c(T(n, i)), \tag{13}$$

$$\frac{\partial T}{\partial t} \to (T(n, i + 1) - T(n, i))/\delta t, \tag{14}$$

$$\frac{\partial^2 T}{\partial z^2} \to \begin{cases} (T(n + 1, i) - 2T(n, i) + T(n - 1, i))/\delta z^2, & n > 0 \\ (T(1, i) - T(0, i))/\delta z^2, & n = 0. \end{cases} \tag{15}$$

The starting temperature is set as $T(n, 0) = 0\,^\circ$C, and the solution of the linear equations marched forward in time, deriving $T(n', i + 1)$ from $T(n, i)$. In the simulations discussed below, we take the spatial and temporal intervals, respectively, to be $\delta z = 1.2$ nm and $\delta t = 0.01$ ps. These satisfy the stability criterion for the parabolic heat diffusion equation[20,21]

$$s = \frac{\kappa\delta t}{\delta z^2} < \frac{1}{2}, \tag{16}$$

with the value of s being 0.475 away from the melting point and even smaller in the region of melting.

Figures 2–4 show results emerging from our thermal simulations. For early times, i.e., the first nanosecond or two, it is mostly just the material near the surface into which the laser beam penetrates that heats up, and the temperature rise more or less mirrors the integrated laser pulse. At slightly later times, with the heat being conducted into the interior of the sample, the surface temperature then lags behind the integrated laser intensity, and this is balanced by the rising temperature in the interior. At later times still, once the laser intensity has passed its maximum, the surface temperature declines and the heat is distributed more and more deeply into the solid. The greater the laser pulse energy J, the greater the maximum temperature reached at the surface and nearby for any value of r.

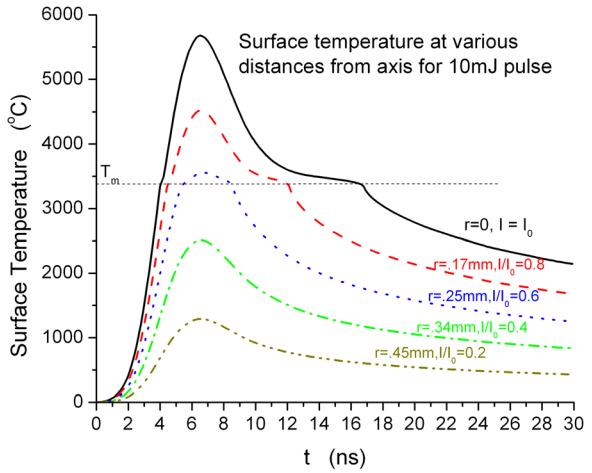

FIG. 2. Laser irradiated surface temperature as function of time at various distances from the axis (i.e., beam center) for a 10 mJ laser pulse and thereby various relative laser intensities $I(r)/I(0)$. For incident relative pulse intensities greater than or equal to 0.6, melting takes place. The first kink corresponds to initiation of melting, the second to re-solidification at surface on cooling.

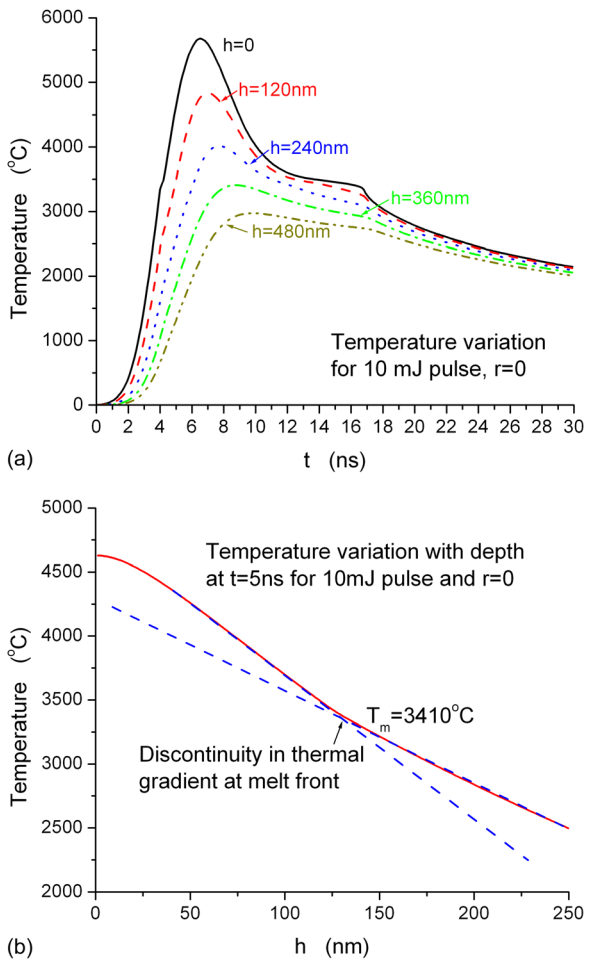

FIG. 3. (a) Temperature variation with time at several depths h below the surface, for $J = 10\,\text{mJ}$, $r = 0$, (b) temperature variation with depth h at $t = 5\,\text{ns}$, showing a discontinuity in the thermal gradient at the melt front. The dashed lines are tangents representing the thermal gradients in the neighboring liquid and solid phases.

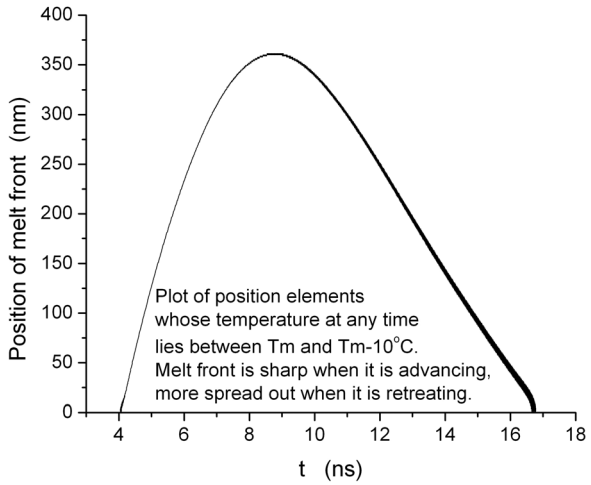

FIG. 4. Depth of melt front as a function of time for a 10 mJ laser pulse at $r = 0$.

At the beam centre for beam radius $d = 0.354\,\text{nm}$ and J exceeding 6 mJ, the maximum temperature near $r = 0$ at the surface and nearby exceeds the melting point, and the temporal variation of the surface temperature shows two rounded kinks (see Figure 2) on passing upwards and downwards through the melting temperature. The first occurs at a time when the laser intensity is high and melting is initiated at the surface. A large fraction of the laser pulse energy is taken up by latent heat of melting as the melt front moves into the interior, and so less is available to raise the temperature and the temperature rises less rapidly. Figure 3(a) shows the temperature variation with time at several depths h, for $J = 10\,\text{mJ}$, $r = 0$. Figure 3(b) shows the temperature variation with depth h at $t = 5\,\text{ns}$, for $J = 10\,\text{mJ}$ and $r = 0$, by which time the melt front has reached a depth of 130 nm. There is a slightly rounded kink in the curve, with change of gradient made obvious by the intersection of the dashed tangents representing the thermal gradients in the neighboring liquid and solid phases. The discontinuity in the gradient comes about because the melt front acts as a heat sink, absorbing or releasing latent heat in the process of moving. The velocity of the melt front is related to the discontinuity in the thermal gradient by[22–24]

$$\rho L \frac{dh_m}{dt} = \left\{ -K_L \frac{\partial T_L}{\partial h}\bigg|_{T_m} + K_S \frac{\partial T_S}{\partial h}\bigg|_{T_m} \right\}, \qquad (17)$$

with $K_L = K_S$ in our simulations. At $t = 8.7\,\text{ns}$, a short while after the laser intensity has passed its maximum and the surface temperature has started declining, the melt front reaches its greatest depth of 365 nm, as shown in Figure 4. The melt front now retreats back to the surface, and in doing so releases latent heat, creating somewhat of a thermal bottleneck for the diffusion of heat from the melt pool. As a result, the surface temperature levels off towards the melting temperature as the re-solidification front approaches the surface, with the velocity of retreat again given by (17). Once solidification is complete, the surface temperature curve kinks downwards.

The above sequence of events is a particular example of what is known as the classical Stephan problem. With suitable

simplifying assumptions, this problem can be treated analytically, and there exists also an extensive literature on computer simulations applied to it, see Ref. 22 and references cited therein. Assuming a rectangular laser pulse and constant material parameters, Tokarev and Kaplan[22] have derived analytic expressions that predict qualitatively the behavior shown in Figure 4 for a wide range of metals.

III. THERMAL STRESSES AND DERIVED SURFACE FORCE DISTRIBUTIONS

A. Radial surface stress

The approach below is predicated on the acoustic emission emanating from a thermally stressed region within a very short distance, of a micron or so, of the surface, as in the tungsten experiments by Reese *et al.*[12] This is sufficiently close to the surface that the relaxation of the normal component of stress is on a time scale shorter than the time resolution of the experiment, which is of the order of a nanosecond. The radius of the laser beam, which is several hundreds of microns, and the plate thickness, which is 3.12 mm, are much larger than this. It is on this basis that locally near the surface, for any given pulse energy J and distance r from the laser beam axis, the heat transport has been treated as a 1D problem. Locally at any value of r, we can consider the near-surface region as stratified into laminae, which undergo thermal expansion normal to the surface but are laterally constrained, thus entering a state of lateral compressive (negative) stress or tensile (positive) stress in the case of a lamina cooling down after re-solidification. For this purpose, we introduce the source function

$$\Im = \dot{T}(h,\tau)\delta(z-h)H(t-\tau), \tag{18}$$

where $\delta(z)$ is the Dirac delta function, $H(t)$ is the unit step function, and $\dot{T}(h,\tau)$ is the time rate of change of the temperature. This source function describes the sudden rise in temperature at time τ of the infinitesimally thin lamina at depth h below the surface by $\dot{T}(h,\tau)$. The temperature profile at r is given in terms of this source function by

$$T(z,t) = \int_0^\infty dh \int_0^t d\tau \dot{T}(h,\tau)\delta(z-h)H(t-\tau). \tag{19}$$

We determine the force distributions that arise from this source function and then integrate over h and τ to obtain the force distributions due to $T(z,t)$.

The source lamina is able to expand freely in the normal direction (this is discussed further in Section III C) but is constrained from expanding laterally, thereby entering a state of lateral compressive thermal strain described by

$$\tilde{\varepsilon}_{xx} = \tilde{\varepsilon}_{yy} = -\alpha\Im, \tag{20}$$

where α is the linear thermal expansion coefficient. From the stress-strain relationship for an isotropic solid, the thermal stresses are given by

$$\begin{aligned}\tilde{\sigma}_{xx} = \tilde{\sigma}_{yy} &= \lambda(\tilde{\varepsilon}_{xx} + \tilde{\varepsilon}_{yy} + \tilde{\varepsilon}_{zz}) + 2\mu\tilde{\varepsilon}_{xx} \\ &= \lambda(-2\alpha\Im + \tilde{\varepsilon}_{zz}) - 2\mu\alpha\Im\end{aligned} \tag{21}$$

and

$$\tilde{\sigma}_{zz} = 0 = \lambda(-2\alpha\Im + \tilde{\varepsilon}_{zz}) + 2\mu\tilde{\varepsilon}_{zz}, \tag{22}$$

where λ and μ are the temperature dependent Lamé elastic constants. Solving these equations, we obtain the radial (lateral) stress

$$\tilde{\sigma}_{rr} = \tilde{\sigma}_{xx} = \tilde{\sigma}_{yy} = -2\mu\xi\Im, \tag{23}$$

where

$$\xi(T) = \left\{\frac{\alpha(3\lambda+2\mu)}{\lambda+2\mu}\right\} = \left(1 - \frac{4\mu}{3C_{11}}\right)\beta, \tag{24}$$

and $\mu(T)$ and $\beta(T)$ have been defined earlier. The thermodynamic stability criterion for solids,[25] $\mu/C_{11} < 3/4$ ensures that $\xi > 0$. Prior to melting $\tilde{\sigma}_{rr}$ is negative (compressive). On entering the molten state, μ and hence $\tilde{\sigma}_{rr}$ are zero. On cooling after re-solidification has taken place, the lamina enters a state of increasing tensile (positive) stress. Integrating (23) over h and τ, we obtain the radial stress at z and t,

$$\begin{aligned}\sigma_{rr}(z,t) &= \int_0^\infty dh \int_0^t d\tau\tilde{\sigma}_{rr} = -2\int_0^\infty dh \int_0^t d\tau\mu\xi\Im \\ &= -2\mu(T)\xi(T) \\ &\quad\times \begin{cases} T; & \text{before melting} \\ 0; & \text{in molten state} \\ T - (T_m - 100\,^\circ\text{C}); & \text{after resolidification.}\end{cases}\end{aligned} \tag{25}$$

B. Radial surface force distribution

Bearing in mind that the radial stress field is confined to a shallow region just below the surface, by integrating $\sigma_{rr}(z,t)$ with respect to z, the result can be regarded as a 2D radial surface stress (force per unit length) acting across a line normal to **r** in the surface

$$\Lambda_{rr}(t) = \int_0^\infty dz\sigma_{rr}(z,t). \tag{26}$$

The calculated compressive radial stress $-\Lambda_{rr}(t)$ at various distances r from the centre of the laser beam and hence intensities I for a 10 mJ pulse and $d = 0.354$ mm is shown in Fig. 5(a). The gradient of this stress

$$F_r(t) = \frac{\partial\Lambda_{rr}}{\partial r} \tag{27}$$

represents the radial force per unit area acting in the surface. In calculating the epicentral displacement response using the Green's function for an infinite continuum, it is convenient,

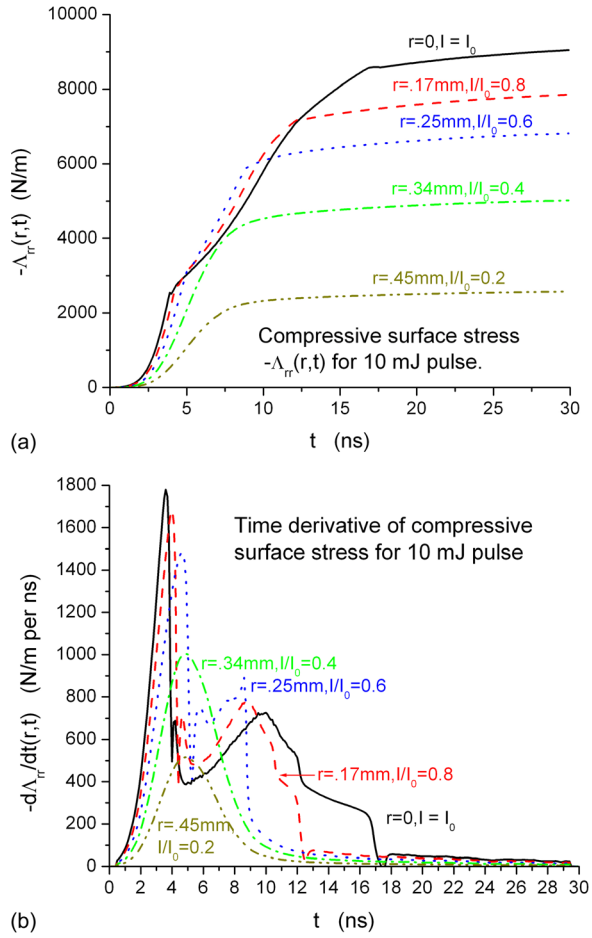

FIG. 5. (a) Compressive radial stress $-\Lambda_{rr}(r,t)$ and (b) its time derivative $-\dot{\Lambda}_{rr}(r,t)$ for 10 mJ Gaussian pulse of radius $d = 0.354$ mm at various distances r from the beam axis. The peak energy density is 25400 J/m^2 and peak power is 228 MW/cm^2.

as we show later, to calculate the response to a step function force and then convolve with F_r using its time derivative

$$\dot{F}_r(t) = \frac{\partial \dot{\Lambda}_{rr}}{\partial r}\,; \quad \dot{\Lambda}_{rr}(t) = \frac{\partial \Lambda_{rr}}{\partial t}. \tag{28}$$

Referring to Fig. 5, in the case of $I/I_0 = 0.4$ and 0.2, the temperature does not reach the melting point, and so all the absorbed energy contributes to $-\Lambda_{rr}(r,t)$, and the time dependence of $-\dot{\Lambda}_{rr}(r,t)$ matches exactly the laser intensity. At the opposite extreme, for $I/I_0 = 1$, to start with $-\Lambda_{rr}(r,t)$ rises rapidly with laser intensity, but when the surface temperature reaches the melting point at 4.0 ns, a large fraction of the absorbed energy flux is taken up as latent heat of melting and subsequent heating of the melt, and $-\Lambda_{rr}(r,t)$ rises less steeply and $-\dot{\Lambda}_{rr}(r,t)$ drops precipitously. Shortly thereafter $-\dot{\Lambda}_{rr}(r,t)$ rises slowly up to about 10 ns, just after the melt front has reached its maximum depth of 385 nm. Between 10 ns and 17 ns, the melt front is retreating and re-solidification is complete at the end of this period. In calculating $-\Lambda_{rr}(r,t)$ in this period, there is partial cancellation between the contribution of never-melted material and re-solidified material, but $-\dot{\Lambda}_{rr}(r,t)$ is still quite large during this time because the latent heat being released is finding its way into un-melted solid. Once re-solidification is complete at 17 ns, the only contribution to $-\Lambda_{rr}(r,t)$ comes from further absorption of laser radiation, which by this time is very weak. The behavior of $-\Lambda_{rr}(r,t)$ and $-\dot{\Lambda}_{rr}(r,t)$ for $I/I_0 = 0.8$ and 0.6 is similar. For all values of I, $-\Lambda_{rr}(r,t)$ approaches a plateau towards 30 ns. The plateau level is proportional to I before melting, but the rise is less rapid once the melt threshold is exceeded, due to the stress relaxation.

C. Normal surface force distribution

In the process of a lamina changing in temperature and expanding in the normal direction, two compressional pulses are launched, one towards the interior and the other towards the free surface of the solid. It takes a time h/c_L, for the latter pulse to reach the surface and be reflected as a dilatational pulse, leaving at all later times the medium between the lamina and the surface with a static outward displacement $\xi\dot{T}(h,\tau)$, which corresponds to the free expansion of the lamina. The dynamic stress field pertaining to the two pulses can be inferred from Eq. (15) of Telschow and Conant[26] and is given by

$$\begin{aligned}\tilde{\sigma}_{zz}(z,t,\tau,h) &= C_{11}\frac{\partial \tilde{w}}{\partial z} \\ &= \frac{\xi C_{11}\dot{T}(h,\tau)}{2c_L}\left\{-\delta\left[t-\tau-\frac{(z-h)}{c_L}\right]\right. \\ &\quad \left.+\,\delta\left[t-\tau-\frac{(z+h)}{c_L}\right]\right\}.\end{aligned} \tag{29}$$

These two pulses can be considered as originating at the surface as a result of an externally impressed positive impulsive force at time $\tau - h/c_L$ and an externally impressed negative impulsive force of equal magnitude at time $\tau + h/c_L$. Thus, in effect there is a force per unit area acting normal to the surface given by

$$\begin{aligned}\tilde{F}_z(t,\tau,h) &= -\tilde{\sigma}_{zz}(z=0,t,\tau,h) \\ &= \frac{\xi C_{11}\dot{T}(h,\tau)}{2c_L}\left\{\delta\left[t-\left(\tau-\frac{h}{c_L}\right)\right]\right. \\ &\quad \left.-\,\delta\left[t-\left(\tau+\frac{h}{c_L}\right)\right]\right\}.\end{aligned} \tag{30}$$

Integrating over τ and h to obtain, the resultant force density for all the laminae yields

$$F_z(t) = \int_0^\infty dh\,\frac{\xi C_{11}}{2c_L}\left\{\left.\frac{\partial T(h,\tau)}{\partial \tau}\right|_{\tau=t+h/c_L} - \left.\frac{\partial T(h,\tau)}{\partial \tau}\right|_{\tau=t-h/c_L}\right\}. \tag{31}$$

Most of the acoustic emission occurs in a distance less than about 500 nm of the surface, where $h/c_L \le 500\,\text{nm} \div 5570\,\text{m/s} \approx 0.1\text{ns}$, which is much less than the time scale for the evolution of the temperature, and so we can approximate the difference between the two terms by $2h/c_L$ times their derivative with respect to τ, yielding

$$F_z(t) = \int_0^\infty dh \frac{\xi C_{11} h}{c_L^2} \frac{\partial^2 T(h,t)}{\partial t^2} = \int_0^\infty dh \xi \rho h \frac{\partial^2 T(h,t)}{\partial t^2}. \quad (32)$$

The above result holds at each value of r, so by solving the heat conduction problem at each r, one obtains $\ddot{T}(r,h,\tau)$, and hence by integration $F_z(r,t)$. In Eq. (32), c_L is in effect the average longitudinal velocity between the surface and the depth h and $C_{11} = \rho \tilde{c}_L^2$, where $\tilde{c}_L$ is the longitudinal velocity at the surface. On the supposition that these two values of the velocity do not differ markedly, we have made the replacement $C_{11}/c_L^2 \to \rho$ in (32). In a more precise modeling of the force generation, $\xi\rho$ could be treated as a local temperature dependent quantity.

Figure 6 shows calculated plots of $F_z(r,t)$ under various circumstances. In the absence of melting, see the 4 mJ curve in Fig. 6(a), it has a smooth bipolar time dependence, which is simply understood from the time dependence of the temperature at any depth, see Fig. 2. Initially $T(t)$ is curved sharply upwards, i.e., $\ddot{T}(t) > 0$. In the temperature interval of a few ns straddling the maximum, $T(t)$ is curved downwards, i.e., $\ddot{T}(t) < 0$, and beyond that $\ddot{T}(t)$ is small and positive but leveling off to zero. This variation is exhibited at all depths h, and thus the roughly bipolar form of $F_z(t)$ from Eq. (32). Melting has a pronounced effect on the normal force distribution $F_z(r,t)$, as shown in Figure 6(a). Sharp dips occur at the times when the melt front is launched into the medium and when the re-solidification front returns to the surface. This is because the $T(t)$ curve is curved sharply downwards at these times, see Figs. 2 and 3, and so $\ddot{T}(t)$ is very large and negative. The volume change on melting also has an important influence on $F_z(r,t)$, because of its dependence on β through ξ. This can be seen in Fig. 6(b).

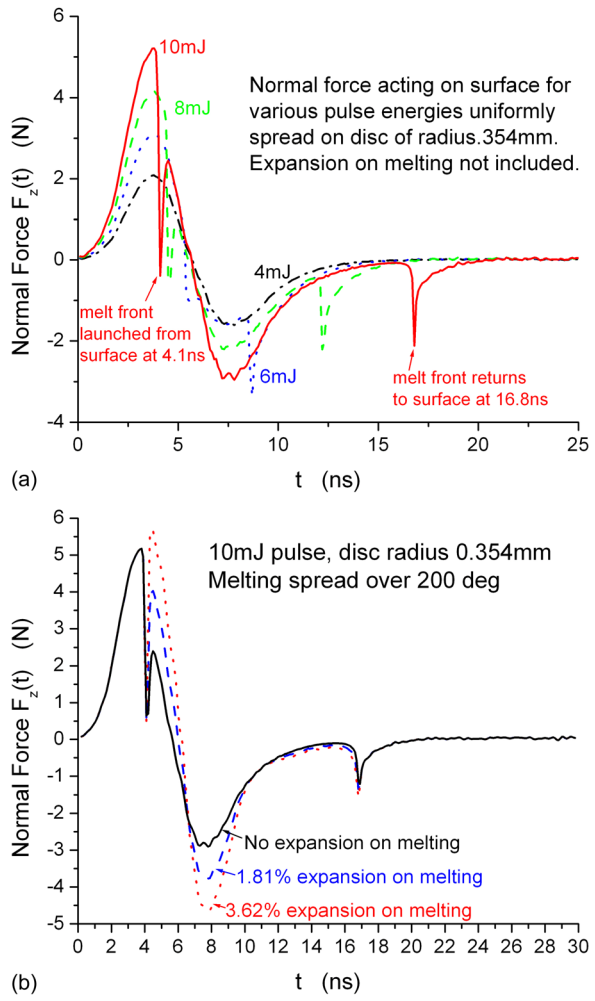

FIG. 6. (a) Normal force $\pi d^2 F_z(0,t)$ time dependence for various laser pulse energies below and above melt threshold. (b) Influence of volume change on melting on the normal force $\pi d^2 F_z(0,t)$.

IV. EPICENTRAL DISPLACEMENT RESPONSE

The epicentral displacement response to the radial and normal force distributions have been calculated using two different approaches, the one being on the basis of elastodynamic Green's functions for plate geometry determined by the Cagniard generalized ray method, and the other by FEM simulations. As will become evident below, the results emerging from the two approaches are in very close agreement, providing validation for the two approaches. The comparative advantage of the generalized ray method is that it is computationally very efficient, while the FEM simulations have the advantage of greater flexibility regarding sample geometry and spatial dependence of materials properties, etc., and as a matter of course yield the evolving elastodynamic field throughout the sample.

A. Convolution of surface force distributions with plate Green's functions

The epicentral displacement caused by the laser heating of the surface is obtained by convolving the force distributions calculated in Sec. III with relevant elastodynamic Green's functions for plate geometry discussed in the Appendix. Since the radial force distribution rises over a period of order 10 ns and then plateaus out, the epicentral displacement $U_z^r(t)$ is obtained by convolving the time derivative of the radial force, $\dot{F}_r(t)$, with $G_{zr}(h,r,t)$, the normal epicentral response to a point radial force on the opposite surface having unit step function time dependence, and then integrating over the illuminated surface area thus

$$U_z^r(t) = \int_0^{3d} dr.2\pi r \int_0^{30\text{ns}} d\tau \dot{F}_r(\tau) G_{zr}(h,r,t-\tau), \quad (33)$$

where the cutoffs in the numerical integrations have been set at $3d = 1.062$ mm (which is divided into 100 intervals) and 30 ns (divided into ns intervals) for r and τ, respectively.

Figure 7 shows the calculated epicentral displacement for the 3.12 mm thick tungsten plate resulting from the radial force distribution for a range of laser pulse energies, based on the assumption of a 4% volume change on melting. The curves are similar in shape to $G_{zr}(h,r,t)$ except for the rounding of the P and S arrivals due to the range of propagation distances ℓ and the finite duration of the laser pulse. The P and S arrivals are initiated close to the minimum times $h/c_L = 560$ ns and $h/c_T = 1010$ ns for longitudinal and shear wave propagation over the distance h from the centre of the

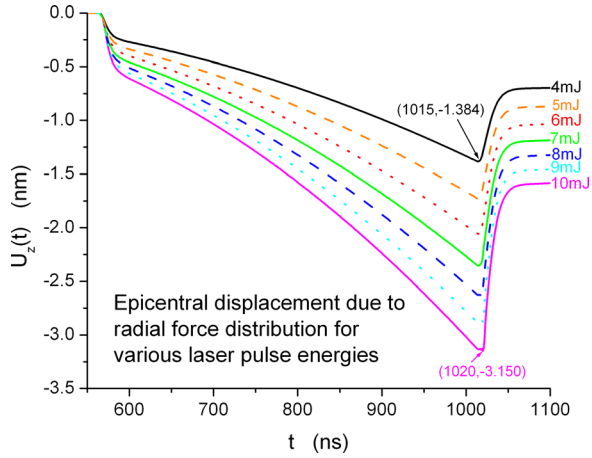

FIG. 7. Calculated epicentral displacement for a 3.12 mm thick tungsten plate resulting from the radial force distribution, for a range of laser pulse energies.

heated spot to the epicentral detection point. Below the melt threshold, the amplitude increases linearly with pulse energy J, and then more slowly above the melt threshold, because of the stress relaxation discussed earlier.

The normal force distribution is in the form of a bipolar pulse that persists for about 10 to 20 ns. The resulting epicentral displacement $U_z^z(t)$ is therefore obtained by convolving the normal force, $F_z(t)$, with the Greens function for a point impulse, which is the time derivative of $G_{zz}(h,r,t)$, and then integrating over the illuminated surface area thus

$$U_z^z(t) = \int_0^{3d} dr.2\pi r \int_0^{30\text{ns}} d\tau F_z(\tau)\dot{G}_{zz}(h,r,t-\tau), \qquad (34)$$

where, as before, the cutoffs in the numerical integrations have been set at $3d$ and 30 ns for r and τ respectively.

Figure 8(a) shows the calculated epicentral displacement $U_z^z(t)$ for the 3.12 mm thick tungsten plate resulting from the normal force distribution for a 10 mJ laser pulse energy. In $\dot{G}_{zz}(h,r,t)$, the P wave arrival take the form of a delta function and discontinuity, while the S arrival takes the form of a delta function of smaller amplitude and a larger discontinuity. On convolving with the normal force distribution, the $U_z^z(t)$ that results displays a somewhat smooth bipolar pulse shape near the P arrival, which mainly arises from the delta function, and which is the customarily referred to precursor. There is also a small negative monopolar pulse at the S arrival which mainly arises from the discontinuity in $\dot{G}_{zz}(h,r,t)$. The sharp temporal features in the force distribution are effectively averaged out in the convolution. In between the P and S arrivals, $U_z^z(t)$ is smaller by a factor on order of $c_L\Delta t/\ell \approx 4\,\text{ns}/550\,\text{ns} < 0.01$, as compared with the precursor displacement. This is to be regarded as a near field effect, in contrast to the displacements at the wave arrivals, which are considered far field effects for a pulse. Fig. 8(b) shows $U_z^z(t)$ for a range of laser pulse energies on an expanded scale in the region of the P arrival. The precursors are all bipolar in shape, with only the one for the 10 mJ pulse showing some structure.

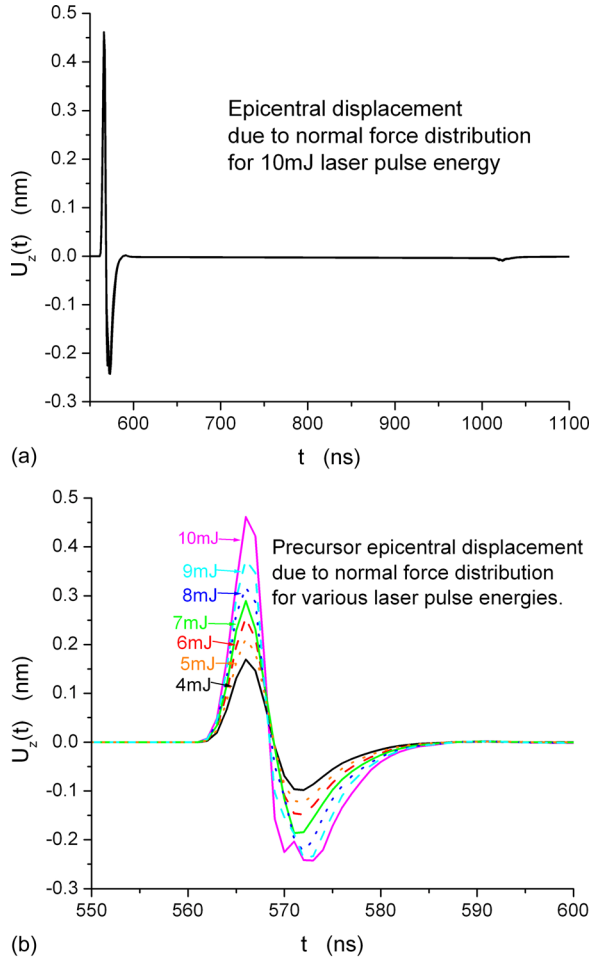

FIG. 8. Calculated epicentral displacement $U_z^z(t)$ for a 3.12 mm thick tungsten plate resulting from the normal force distribution for (a) 10 mJ laser pulse energy, and (b) for a range of pulse energies on an expanded scale in the region of the P arrival.

Figure 9(a) shows the combined epicentral displacement $U_z^r(t) + U_z^z(t)$ due to the radial and normal surface force distributions for a Gaussian pulse of radius $d = 0.354$ mm and a number of different laser pulse energies J, while Fig. 9(b) shows a blow up of the region around the precursor, and Fig. 9(c) is a blowup of the region near the S arrival. The negative dip of the precursor is largely obscured in the combining of the two displacements, and the precursor is more monopolar in appearance, a phenomenon that can be seen in the results of, e.g., Refs. 27 and 28.

B. FEM calculation of epicentral displacement response to surface force distributions

Quite independently we have used the commercial Finite Element package (PzFlex, Weidlinger Asc.) to simulate the elastodynamic field in the 3.12 mm thick tungsten plate arising from the force distributions given by Eqs. (27) and (32). The material properties assumed were the same as those used above.

Due to the axial symmetry of the problem, we have modeled the 3.12 mm thick plate by considering only a 2D section of the plate of 4 mm width and applying absorbing boundary conditions. The square grid of the model consisted

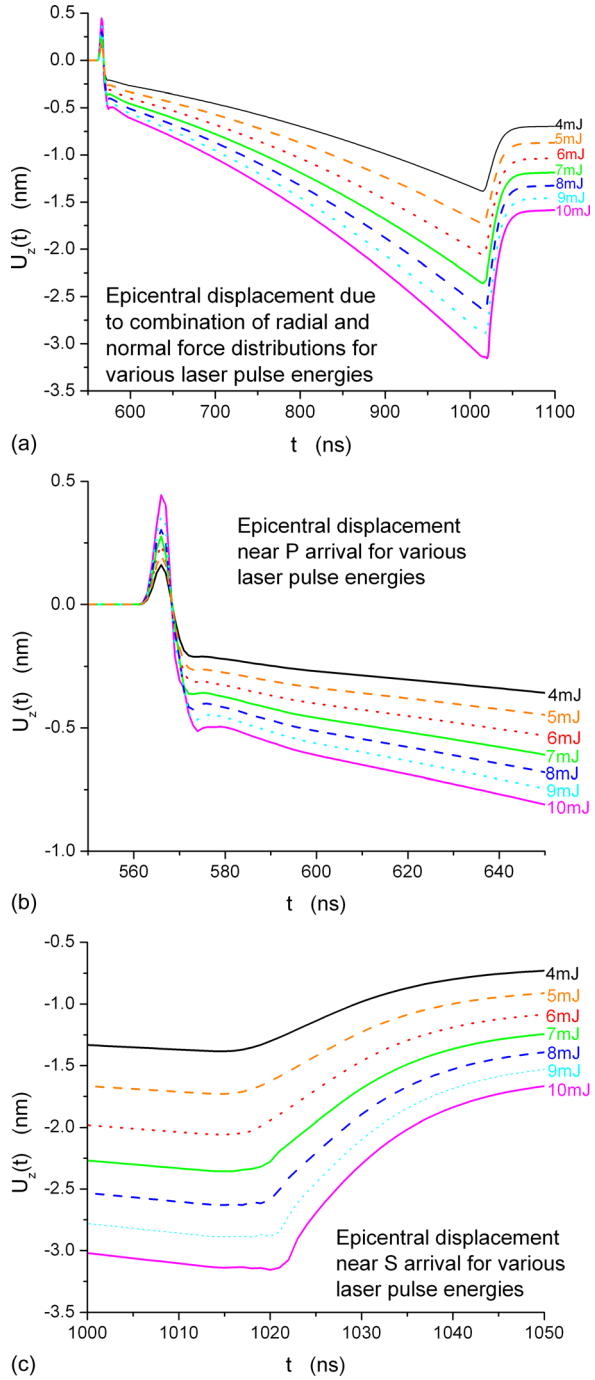

FIG. 9. (a) Combined epicentral displacement $U_z^r(t) + U_z^z(t)$ for a range of laser pulse energies, (b) blowup of region near P arrival and (c) blowup of region near S arrival.

of 5334 × 4161 nodes corresponding to ∼44.4 × 10^6 degrees of freedom (DOFs) with $dx = dy = 0.75\ \mu$m. The time step of $dt = 108$ ps was determined from the stability criterion for explicit temporal integration.[29] The total duration of the simulation was $T_{total} = 1150$ ns, determined by the arrival of the shear wave (at ∼1020 ns after the generation). The calculation was parallelized across 5 computational cores and required ∼2 h on a Windows 64 bit platform (Intel Xeon(R) CPU 2.40 GHz). The surface force distributions were spatially and temporally interpolated on the computational grid. In Sec. III, the surface forces were evaluated only for 30 ns; the thermal stresses persist, however, for much longer. This effect was taken into account by keeping the surface stresses constant after 30 ns.

The epicentral displacement response to a 10 mJ laser pulse of radius $d = 0.354$ mm is shown in Fig. 10(b). The Green's function results are compared with those of the FEM numerical simulation, showing very close agreement, as can be seen.

Numerical simulations also allow a simple visualization of the elastodynamic field in the time domain. This is shown in Figure 11, which depicts the magnitude of the particle velocities. In the lower region of Fig. 11(a), there is a sharp pulse, concentrated near epicenter, and approaching the detection surface at the longitudinal velocity. This represents mainly the precursor displacement which arises from the normal force distribution, which is a maximum near the axis (see Fig. 10(a)). On either side of the precursor pulse are two roughly circular, somewhat more diffuse pulses, which arise from the radial force distribution. The reason for the splitting is that, disregarding melting for the moment, the radial surface stress field exciting these waves varies as $\exp(-r^2/d^2)$, and so the radial force density is a maximum at $r = d/\sqrt{2} = 0.25$ mm (see Fig. 10(a)). The position of this maximum in the force density is moved slightly further out by melting. So in the sections shown in Fig. 11, there are in effect two sources separated by about 0.5 mm. The directivity pattern for P waves radiated by a radial force is zero

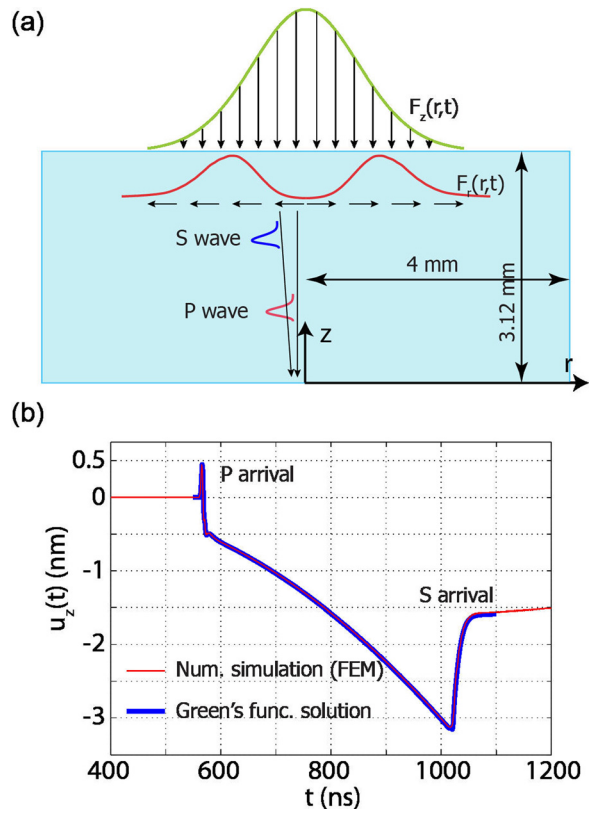

FIG. 10. (a) Representation of the model for the propagation of elastic waves generated by pulsed laser. (b) Comparison between FEM numerical simulation and Green's function calculated normal surface displacement response at epicenter of a 3.12 mm thick tungsten plate, to the radial and normal force distributions arising from a 10 mJ pulse with $d = 0.354$ mm. The two curves are in very close agreement.

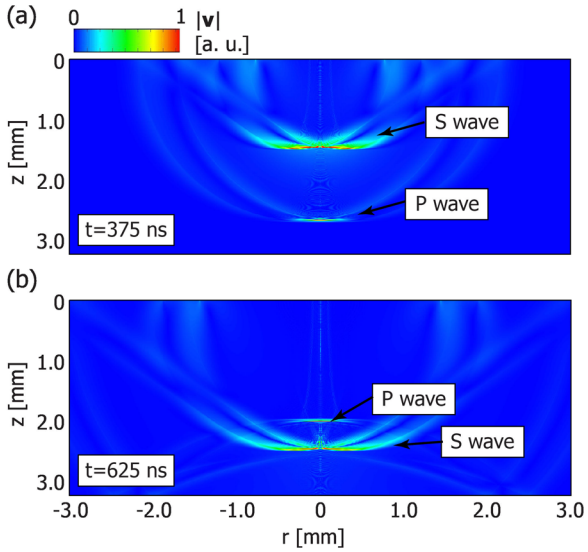

FIG. 11. Visualization of the wave field (magnitude of the velocity $|\mathbf{v}|$) in the far field at (a) 375 ns after the start of the 10 mJ pulse and (b) 625 ns after the start, by which time the still sharp P wave precursor has been reflected.

directly downwards, and this is evident in the leading wave. In Figs. 11(a) and 11(b), one can also see the split and more diffuse S waves arising from the radial force distribution. These waves are at their most intense near to epicenter, because the directivity pattern for S waves radiated by a horizontal force is at a maximum vertically downwards.

As a further comparison between the Green's function and FEM results, we have calculated the epicentral wave forms due to the normal force distributions for 4, 6, 7, 8, 9, and 10 mJ pulses. Due to the axial symmetry of the problem, we have modeled the 3.12 mm thick plate by considering only a 2D section of the plate of 2 mm width and applying absorbing boundary conditions. The square grid consisted of 3334×5201 nodes corresponding to $\sim 34.7 \times 10^6$ DOFs with $dx = dy = 0.60\,\mu$m and $dt = 86$ ps. The total duration of the simulation was $T_{total} = 800$ ns, determined by the arrival of the bulk longitudinal wave at ~560 ns after triggering. The computational parameters were similar to the first simulation by parallelizing across 5 computational cores with ~2 h computational time on a Windows 64 bit platform (Intel Xeon(R) CPU 2.40 GHz). The numerically evaluated epicentral wave forms due to the normal force are shown in Fig. 12 and show very close agreement with the Green's function results (Fig. 8(b)).

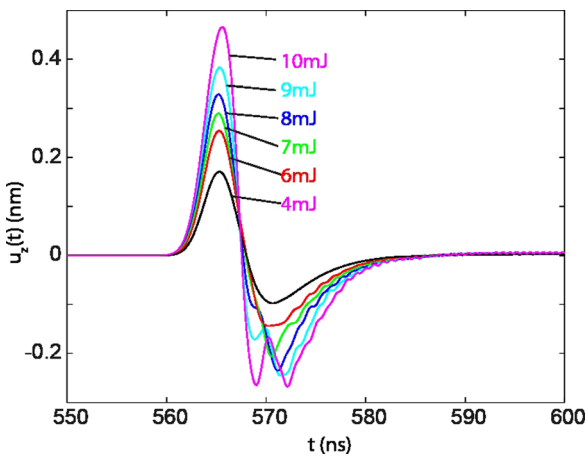

FIG. 12. FEM calculated epicentral wave forms near the P arrival due to the normal force distributions for 4, 6, 7, 8, 9, and 10 mJ laser pulses.

V. DISCUSSION AND CONCLUSIONS

The simulations indicate that the precursor arrival time is insensitive to the occurrence of melting, but that the S arrival time moves later once melting starts, by up to 5.5 ns for the range of pulse energies calculated for (see Figure 13(b)). This is consistent with the trend observed by Reese *et al.*[12] but not in quantitative agreement with the magnitude of shift they observed. The variation of the maximum positive displacement of the precursor $u_{max}(J)$ and the maximum negative displacement $u_{min}(J)$ near the T arrival time is more pronounced. While proportional to J below the melt threshold, they show more complicated behavior once melting takes place. Figure 13(a) shows plots of the relative variations of these quantities, expressed as $\frac{u_{max}(J)}{J.u_{max}(1)}$ and $\frac{u_{min}(J)}{J.u_{min}(1)}$, below and above the melt threshold. The slower growth in $u_{min}(J)$ with J above the melt threshold is because of the stress relaxation by the melt. The initially slower growth in $u_{max}(J)$ once the melt threshold has been exceeded comes

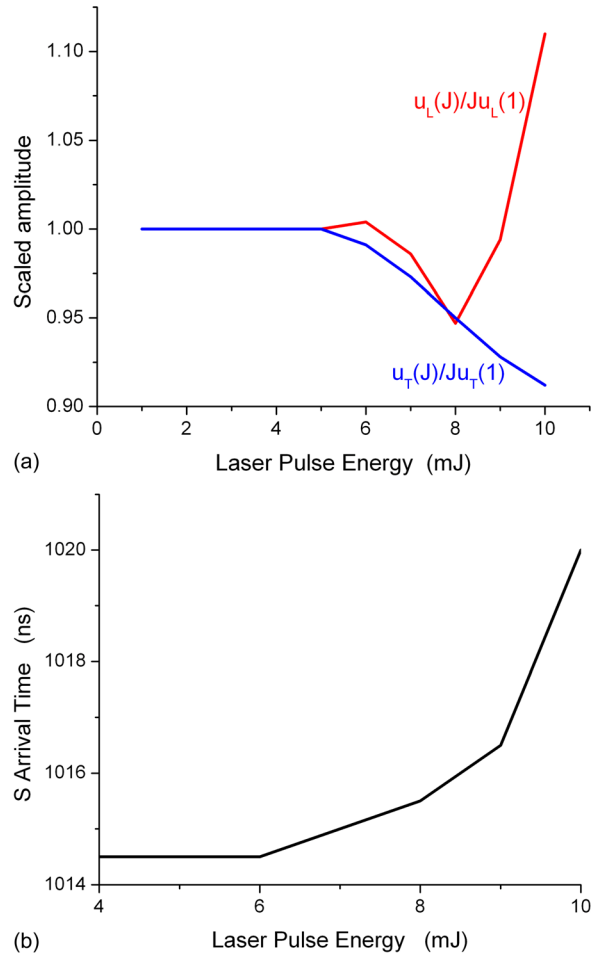

FIG. 13. Effect of melting on (a) the precursor amplitude and amplitude at the S arrival and (b) the S arrival time.

about because much of the heat being absorbed is routed into latent heat, but the associated expansion occurs at the surface where it makes little contribution to the normal force, as can be inferred from the factor h in Eq. (32). For larger J, the melt front penetrates further into the sample, the thermal expansion on melting engenders a larger normal force, and so the precursor amplitude is proportionately larger. This behavior of the two amplitudes is consistent with the experimental observations of Mesaros *et al.*[11] on the effect of melting on laser ultrasound in stainless steel.

The simulations reported in this paper have been based on somewhat idealized assumptions regarding the thermophysical properties of tungsten, with the purpose of illustrating basic concepts not encumbered by too much detail. Future simulations of laser-ultrasound in the melt regime would benefit from invoking more measured thermophysical data from the literature (see, e.g., Refs. 30–34). In treating thermoelastic generation in the transition region from solid to liquid, this paper bridges the subjects of laser-ultrasound in solids and in liquids.[35]

ACKNOWLEDGMENTS

A.G.E. thanks Richard L. Weaver for helpful suggestions. Financial support was provided by 055 Program Fund Grant of Kazakhstan Ministry of Education and Science, by Seed Grant of Nazarbayev University Corporate Fund "Fund of Social Development," the South African National Research Foundation, an ongoing research program of the FWF Austrian Science Fund under the Lise Meitner Position M 1298-N20, the European Regional Development Fund (EFRE) in the framework of the European Union program Regio 13 and the federal state of Upper Austria.

APPENDIX: CAGNIARD GENERALIZED RAY METHOD

The Cagniard generalized ray method is expounded in detail in Refs. 36–39. Our tailoring of this method to the calculation of the early-time elastodynamic Green's functions $G_{zz}(h,r,t)$ and $G_{rz}(h,r,t)$ for a plate of thickness h is briefly summarized here. $G_{zz}(h,r,t)$ denotes the normal displacement response at distance r from epicenter on the lower surface and at time t to a unit normal point force having step function time dependence $H(t)$, applied along the z-axis to the upper surface, while $G_{rz}(h,r,t)$ denotes the radial displacement response. By reciprocity, the epicentral normal displacement response to a radial force applied on the opposite surface a distance r from the z-axis is $G_{zr}(h,r,t) = -G_{rz}(h,r,t)$, the negative sign coming about because we consider a normal force as into the surface but normal displacement as out of the surface. The previously calculated force distributions for a given laser pulse energy are then convolved with the corresponding Green's functions to give the required time dependent epicentral normal displacement.

The axisymmetric displacement response of a plate subjected to a point normal force at the origin on the upper surface can be expressed in terms of two potentials Φ and Ψ, which satisfy the scalar wave equation for longitudinal and shear wave motion, respectively. These partial differential equations are converted to ordinary differential equations by Laplace transforming and the particular solution that satisfies the boundary conditions obtained. The normal and radial displacement responses at the opposite side of the plate are then obtained from these potentials in the form of a sum of generalized ray expressions. Considering just the early arriving direct transmission (and not later arriving reflections), the Laplace transformed displacement response is given by a sum of two terms in the L and S velocities $\gamma = c_L, c_T$ thus[38,39]

$$\tilde{G}_{jz}(h,r,s) = -\frac{1}{\pi\mu}\sum_{\gamma=c_L,c_T}\int_0^\infty J_n(s\xi r)\left\{\frac{E_{\gamma j}\exp(-s\psi_\gamma h)}{\Omega}\right\}\xi\psi_{c_L}d\xi, \tag{A1}$$

where j stands for z or r,

$$\psi_\gamma = \left(\xi^2 + 1/\gamma^2\right)^{1/2}, \tag{A2}$$

$$\Omega = c_T^2((2\xi^2 + 1/c_T^2)^2 - 4\xi^2\psi_{c_L}\psi_{c_T})^2, \tag{A3}$$

$$E_{c_Lz} = -\left(2\xi^2 + 1/c_T^2\right)^2, \tag{A4}$$

$$E_{c_Tz} = 4\xi^2\psi_{c_L}\psi_{c_T}, \tag{A5}$$

$$E_{c_Lr} = -2\left(2\xi^2 + 1/c_T^2\right)\xi\psi_{c_T}, \tag{A6}$$

$$E_{c_Tr} = 2\left(2\xi^2 + 1/c_T^2\right)\xi\psi_{c_T}, \tag{A7}$$

and $J_n(s\xi r)$ are Bessel functions of order $n = 0$ for $j = z$, and $n = 1$ for $j = r$. A crucial step is invoking the integral representations for the Bessel functions

$$J_0(s\xi r) = \frac{2}{\pi}\mathrm{Re}\int_0^{\pi/2}\exp(is\xi r\cos\omega)d\omega, \tag{A8}$$

$$J_1(s\xi r) = \frac{2}{\pi}\mathrm{Im}\int_0^{\pi/2}\exp(is\xi r\cos\omega)\cos\omega\, d\omega. \tag{A9}$$

The Cagniard method is then to regard ξ as a complex variable and transform to another complex variable t, which excluding reflections and considering just the earliest direct wave arrivals at the detection surface, is given by

$$t = -i\xi r\cos\omega + h\psi_\gamma, \tag{A10}$$

for each of the two integral in Eq. (A1). The locus traced out by t with this substitution is in the lower right hand quadrant of the complex plane starting from the point h/γ. This contour can be deformed to run parallel to, and just below the real axis, from its starting point to infinity. With this change of variable, and interchanging the order of integration, Eq. (A1) is transformed to

$$\tilde{G}_{jz}(h,r,s) = \sum_{\gamma=c_L,c_T} \int_{h/\gamma}^{\infty} \left\{ \frac{-2}{\pi^2\mu} \mathrm{Re\,Im} \int_0^{\pi/2} \frac{E_{\gamma j}(\xi)}{\Omega} \frac{d\xi}{dt} \xi \psi_{c_L} \cos^n \omega \, d\omega \right\} \exp(-st)dt$$

$$= \int_0^{\infty} \left\{ \sum_{\gamma=c_L,c_T} \frac{-2H(t-h/\gamma)}{\pi^2\mu} \mathrm{Re\,Im} \int_0^{\pi/2} \frac{E_{\gamma j}(\xi)}{\Omega} \frac{d\xi}{dt} \xi \psi_{c_L} \cos^n \omega \, d\omega \right\} \exp(-st)dt, \quad \text{(A11)}$$

where ReIm stands for real part in the case of $j = z$, $n = 0$, and imaginary part in the case of $j = r$, $n = 1$, and ξ in the integrand is expressed as a function of t by

$$\xi(t) = \frac{irt\cos\omega + h\sqrt{t^2 - (h^2 + r^2\cos^2\omega)/\gamma^2}}{(h^2 + r^2\cos^2\omega)}. \quad \text{(A12)}$$

Thus, in (A11) we see $\tilde{G}_{jz}(h,r,s)$ cast in the form of a Laplace transform $\int_0^{\infty} f(t)\exp(-st)dt$ of a quantity which can hence be identified as the time domain Green's function, i.e.,

$$G_{jz}(h,r,t) = \sum_{\gamma=c_L,c_T} \frac{-2H(t-h/\gamma)}{\pi^2\mu} \mathrm{Re\,Im} \times \int_0^{\pi/2} \frac{E_{\gamma j}(\xi)}{\Omega} \frac{d\xi}{dt} \xi \psi_{c_L} \cos^n \omega \, d\omega \,. \quad \text{(A13)}$$

To avoid singular behavior in conducting the integration over ω numerically, t is ascribed a small negative imaginary part. More complicated problems involving multi-layers and/or reflections are preferably handled by a change of integration variable from ω to the complex quantity ξ,[38] but there is no advantage to gained from this for our purposes.

Figures 14(a) and 14(b) show calculated Greens functions $G_{zr}(h,r,t)$ and $G_{zz}(h,r,t)$, respectively, for a $h = 3.12$ mm thick tungsten plate and three different distances r of the response point from epicenter. Both Green's functions exhibit wave arrival discontinuities and changes in slope at the P arrival at $t_L = \ell/c_L = \sqrt{h^2 + r^2}/c_L$, and the S arrival at $t_T = \ell/c_T = \sqrt{h^2 + r^2}/c_T$. The discontinuities are far-field effects which can be accounted for on the basis of the stationary phase approximation applied to the neighborhood of points on the longitudinal and shear sheets of the acoustic slowness surface where their surface normal points in the observation direction.[40] The overall amplitude of $G_{zr}(h,r,t)$ is zero at $r = 0$, and increases initially as $\sin\theta = r/\ell$, where θ is the angular displacement between force and response points. The overall amplitude of $G_{zz}(h,r,t)$ falls off gradually with angular displacement from epicenter, to start with as $\cos^3\theta$, while the discontinuity at the S arrival is zero at epicenter and then grows initially as $\sin^2\theta$ with angular displacement.

The magnifying effect of the free surfaces on the dynamic response is demonstrated in Figs. 15(a) and 15(b), which depict calculated infinite continuum,[41] half space and plate Green's functions $G_{zr}(h,r,t)$ and $G_{zz}(h,r,t)$, respectively, for tungsten, taking $h = 3.12$ mm and $r = 0.25$ mm, i.e., a point close enough to epicenter that there is no head wave. The overall shape of the responses for the three geometries is similar, with exactly the same wave arrival times, but the amplitudes differ significantly. When a plane wave is incident normally on a free surface, the surface displacement is twice the wave amplitude, and so one might expect the infinite continuum, half space, and plate response amplitudes to be more or less in the ratio [1,2,4]. In fact, comparing the results in Fig. 15, one finds that the P arrival discontinuities of $G_{zz}(h,r,t)$ and some of the other discontinuities conform closely to this expectation, while overall the amplitude ratios range between [1,2,4] and [1,2.44,6.36]. Further from epicenter, beyond the critical angle $\arcsin(c_T/c_L)$, one encounters a head wave arrival in the half space and plate responses which, since it arises at the surface, is not present in the infinite continuum response.

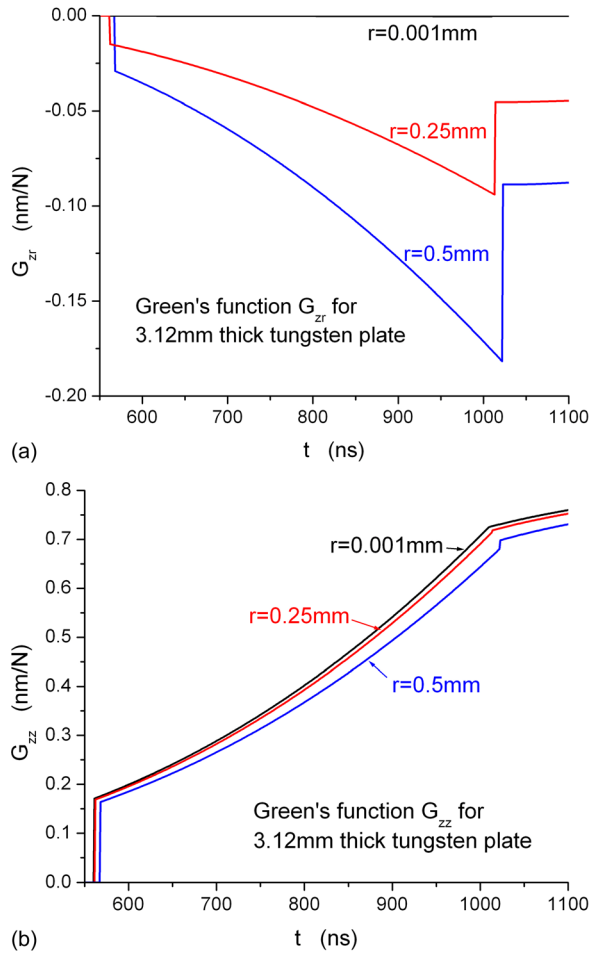

FIG. 14. Calculated Greens functions (a) $G_{zr}(h,r,t)$ and (b) $G_{zz}(h,r,t)$ for a $h = 3.12$ mm thick tungsten plate and three different distances r.

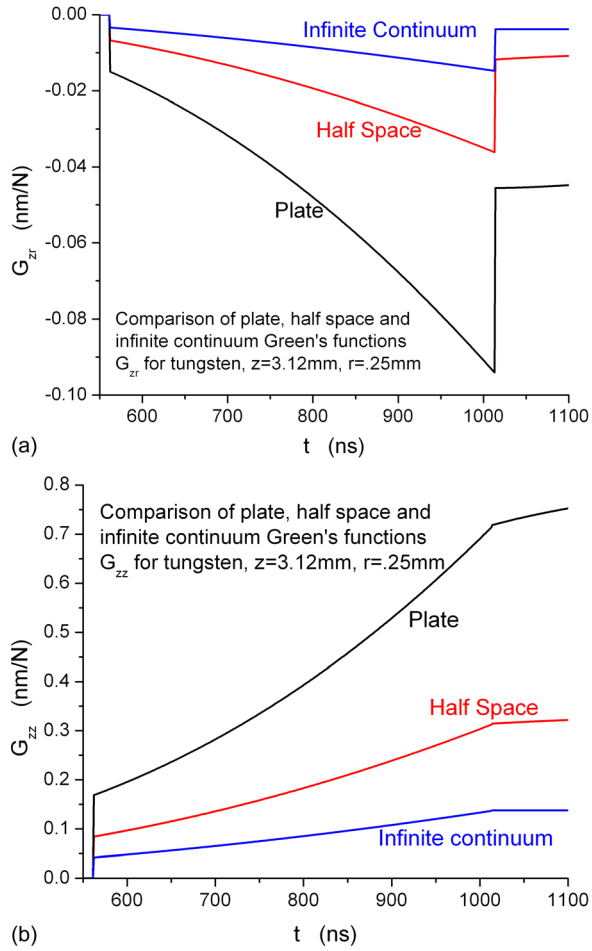

FIG. 15. Calculated infinite continuum, half space and plate Green's functions (a) $G_{zr}(h,r,t)$ and (b) $G_{zz}(h,r,t)$ for tungsten, taking $h = 3.12$ mm and $r = 0.25$ mm.

[1]S. J. Davies, C. Edwards, G. S. Taylor, and S. B. Palmer, "Laser-generated ultrasound: Its properties, mechanisms and multifarious applications," J. Phys. D **26**, 329–348 (1993).

[2]L. F. R. Rose, "Point-source representation for laser-generated ultrasound," J. Acoust. Soc. Am. **75**, 723–732 (1984).

[3]L. F. Bresse and D. A. Hutchins, "Transient generation by a wide thermoelastic source at a solid surface," J. Appl. Phys. **65**, 1441–1446 (1989).

[4]D. A. Hutchins, "Ultrasonic generation by pulsed lasers," in *Physical Acoustics*, edited by W. P. Mason and R. N. Thurston (Academic Press, New York, 1988), Vol. XVIII, p. 21.

[5]C. B. Scruby, R. J. Dewhurst, D. A. Hutchins, and S. B. Palmer, "Laser generation of ultrasound in metals," in *Research Techniques in Nondestructive Testing* (Academic Press, New York, 1982), Vol. V, pp. 281–327.

[6]B. Castagnede and Y. Berthelot, "Photoacoustic interactions by modulation of laser impact; Applications in mechanics and physics of anisotropic solids," J. Acoust. **5**, 417–453 (1992), available at http://perso.univ-lemans.fr/~bcasta/Publications%20journaux/JAcous-5-1992.pdf.

[7]L. Wu, J. C. Chen, and S.-Y Zhang, "Mechanisms of laser-generated ultrasound in plates," J. Phys. D: Appl. Phys. **28**, 957–964 (1995).

[8]S. Fassbender, B. Hoffmann, and W. Arnold, "Efficient generation of acoustic pressure waves by short laser pulses," Mater. Sci. Eng. A **122**, 37–41 (1989).

[9]A. Hoffmann and W. Arnold, "Modeling of the ablation source in laser-ultrasonics," AIP Conf. Proc. **509**, 279–286 (2000).

[10]V. Gusev, A. A. Kolomenskii, and P. Hess, "Effect of melting on the excitation of surface acoustic wave pulses by UV nanosecond laser pulses in silicon," Appl. Phys. A **61**, 285–298 (1995).

[11]M. Mesaros, O. E. Martinez, G. M. Bilmes, and J. O. Tocho, "Acoustic detection of laser induced melting of metals," J. Appl. Phys. **81**, 1014–1016 (1997).

[12]S. J. Reese, Z. N. Utegulov, F. Farzbod, R. S. Schley, and D. H. Hurley, "Examination of the epicentral waveform for laser ultrasound in the melting regime," Ultrasonics **53**, 799–802 (2013).

[13]R. D. Larrabee, "The spectral emissivity and optical properties of tungsten," Technical Report 328, Research Laboratory of Electronics, MIT, May 21, 1957.

[14]See http://www.plansee.com/en/Materials-Tungsten-403.htm#Thermophysikalische_Wolfram.

[15]See http://www.engineeringtoolbox.com/fusion-heat-metals-d_1266.html.

[16]See http://en.wikipedia.org/wiki/Tungsten.

[17]R. Cerny and P. Prikryl, "A computational model of laser-induced melting and solidification with density change," Comput. Phys. Commun. **73**, 179–191 (1992).

[18]H. M. Lu and Q. Jiang, "Melting volume changes of different crystalline lattices," Phys. Status Solidi B **241**, 2472–2476 (2004).

[19]J. E. Parrott and A. D. Stuckes, *Thermal Conductivity of Solids* (Pion, London, 1975).

[20]J. C. Strikwerda, *Finite Difference Schemes and Partial Differential Equations* (SIAM, Philadelphia, 2004).

[21]J. F. Botha and G. F. Pinder, *Fundamental Concepts in the Numerical Solution of Differential Equations* (John Wiley, 1983).

[22]V. N. Tokarev and A. F. H. Kaplan, "An analytical modeling of time dependent pulsed laser melting," J Appl. Phys. **86**, 2836–2846 (1999).

[23]S. L. Sobolev, "Two-temperature Stefan problem," Phys. Lett. A **197**, 243–246 (1995).

[24]K. Mastanaiah, "On the numerical solution of phase change problems in transient non-linear heat conduction," Int. J. Numer. Methods Eng. **10**, 833–844 (1976).

[25]A. G. Every, "The elastic properties of solids: Static and dynamic principles," in *Handbook of Solids, Liquids, and Gases*, edited by M. Levy, H. E. Bass, and R. R. Stern (Academic Press, San Diego, 2001), Vol. I, Chap. 1, pp. 3–36.

[26]K. L. Telschow and R. J. Conant, "Optical and thermal parameter effects on laser generated ultrasound," J. Acoust. Soc. Am. **88**, 1494–1502 (1990).

[27]P. A. Doyle, "On epicentral waveforms for laser-generated ultrasound," J. Phys. D: Appl. Phys. **19**, 1613–1623 (1986).

[28]F. A. McDonald, "On the precursor in laser-generated ultrasound waveforms in metals," Appl. Phys. Lett. **56**, 230–232 (1990).

[29]I. A. Veres, Ultrasonics **50**(3), 431–438 (2010).

[30]G. Grimvall, M. Thiessen, and A. F. Guillermet, "Thermodynamic properties of tungsten," Phys. Rev. B **36**, 7816–7826 (1987).

[31]R. S. Hixson and M. A. Winkler, "Thermophysical properties of solid and liquid tungsten," Int. J. Thermophys. **11**, 709–718 (1990).

[32]E. Fraizier, M.-H. Nadal, and R. Oltra, "Noncontact determination of the elastic moduli of β-Sn up and through the melting point," J. Appl. Phys. **93**, 649–654 (2003).

[33]M.-H. Nadal, C. Hubert, and R. Oltra, "High temperature shear modulus determination using a laser-ultrasonic surface acoustic-wave device," J. Appl. Phys. **106**, 024906-1–6 (2009).

[34]C.-K. Jen, J.-W. Liaw, T.-F. Chen, A. Moreau, J.-P. Monchalin, and C.-C. Yang, "Ultrasonic evaluation of semi-solid metals during processing," Meas. Sci. Technol. **11**, 1570–1575 (2000).

[35]L. M. Lyamshev and L. V Sedov, "Optical generation of sound in a liquid; thermal mechanism (review)," Sov. Phys. Acoust. **27**(1), 4–18 (1981) [Akust. Zh. **27**, 5–29 (1981) (in Russian)].

[36]L. Knopoff, "Surface motions of a thick plate," J. Appl. Phys. **29**, 661–670 (1958).

[37]Y.-H. Pao, R. R. Gajewski, and A. N. Ceranoglu, "Acoustic emission and transient waves in an elastic plate," J. Acoust. Soc. Am. **65**, 96–105 (1979).

[38]Y.-H. Pao and R. R. Gajewski, "The generalized ray theory and transient responses of layered elastic solids," in *Physical Acoustics*, edited by W. P. Mason (Academic Press, New York, 1977), Vol. XIII, Chap. 6, pp. 183–265.

[39]A. N. Ceranoglu and Y.-H. Pao, "Propagation of elastic pulses and acoustic emission in a plate," J. Appl. Mech. - Trans ASME **48**(1), 125–132 (1981).

[40]A. G. Every and K. Y. Kim, "Time domain dynamic response functions of elastically anisotropic solids," J. Acoust. Soc. Am. **95**, 2505–2516 (1994).

[41]K. Aki and P. G. Richards, *Quantitative Seismology* (University Science Books, Sausalito, 2002).